ACS NANO

www.acsnano.org

ARTICLE

Triple-Responsive Soft Actuator with Plastically Retentive Deformation and Magnetically Programmable Recovery

Wenwen Li,[¶] Min Sang,[¶] Congcong Lou, Guojiang Liao,* Shuai Liu, Jianpeng Wu, Xinglong Gong,* Qian Ma, and Shouhu Xuan*

Cite This: *ACS Nano* 2023, 17, 24042−24054

Read Online

ACCESS | Metrics & More | Article Recommendations | Supporting Information

ABSTRACT: **Multistimuli responsiveness and programmable shape recovery are crucial for soft actuators in soft robotics, electronics, and wearables. However, existing strategies for actuation cannot attain power-free shape retention after removing the external energy supply. Here, a self-assembled density deposition method was developed to fabricate an electrothermal-NIR-magnetic triple-response actuator which was composed of cellulose nanofiber/poly(vinyl alcohol)/liquid metal (CNF/PVA/LM) and magnetic polydimethylsiloxane (MPDMS) layer. Interestingly, the large deformation can be controllably fixed and the temporary configuration will be programmable recovered under a magnetic field due to the thermal-plastic transferring behavior of the CNF/PVA/LM. Rolling robot prepared based on soft actuators exhibits good ability to avoid obstacles. In addition, the object handling and programmable release capabilities of the carrier robots demonstrate that this actuation approach will contribute to a better understanding of how to more rationally utilize various stimuli for application purposes.**

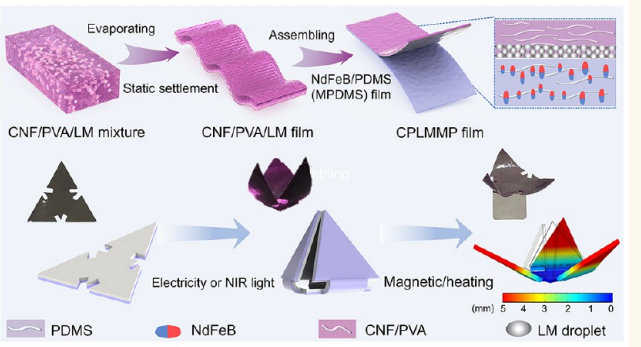

KEYWORDS: *actuator, electrothermal, magnetic, photothermal, programmable*

INTRODUCTION

Soft actuators have attracted much attention due to their effective applications in biomedicine, long-distance transportation, underwater detection, camouflage, and perception technology.[1−3] Different from traditional rigid actuators, the softness and high deformability of soft actuators enable them to morph the body, easily reconfiguring and deforming around object contours.[4,5] Thus far, substantial efforts have been devoted to developing the driving methods of actuators, including temperature,[6] light,[7] pH,[8] humidity,[9] and electric[10] and magnetic fields.[11] Among various types of stimulation, magnetically controlled soft actuators possess great potential for biomedical applications due to their fast response and contactless control performance.[12−14] However, traditional magnetically responsive soft robots require the use of three-dimensional magnetic fields to control their motion, which greatly limits their practical applications. Due to the recoverable characteristics of the magnetic elastomers, magnetically responsive actuators pertain to their unceasing reliance on a constant supply of stimulus sources to operate. Once the stimulus source is removed, the deformations promptly return to the original state. Thus, such soft actuators are unable to maintain any intermediate state configuration without a constant supply of stimuli. However, in practical applications, such as controllable fixtures, handling robots, etc., soft actuators that can achieve shape control with zero energy and control motion with a simple magnetic field can better cope with complex application environments.

To address these limitations, it is highly desirable to design soft robots that can lock onto a desired target shape without relying on a continuous external energy supply. To date, soft actuators based on magnetic shape memory polymers (M-SMPs) have recently come to fore due to their shape can be maintained without the need of a continuous external energy supply.[15,16] For example, Ze et al.[17] mixed two kinds of

Received: September 18, 2023
Revised: November 16, 2023
Accepted: November 17, 2023
Published: November 21, 2023

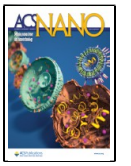

Downloaded via UNIV SCIENCE AND TECHNOLOGY CHINA on February 1, 2024 at 07:03:13 (UTC).
See https://pubs.acs.org/sharingguidelines for options on how to legitimately share published articles.

ACS Publications

© 2023 American Chemical Society

https://doi.org/10.1021/acsnano.3c08888
ACS Nano 2023, 17, 24042−24054

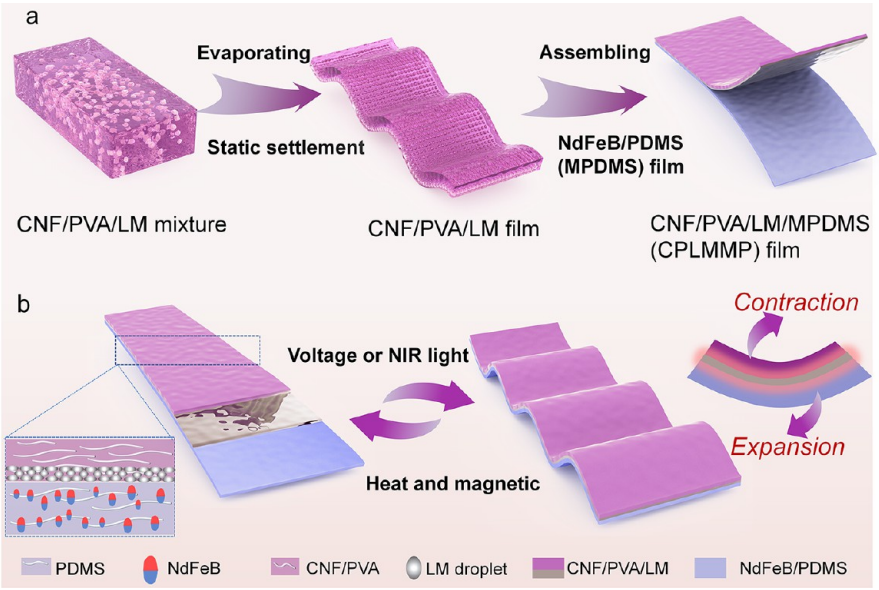

Figure 1. Preparation and driving mechanism of CNF/PVA/LM/MPDMS(CPLMMP) film. (a) Schematic diagram for preparation of CPLMMP film. (b) Schematic diagram of CPLMMP actuator deformation under external electric or NIR light stimulation and shape recovery under magnetic stimulation in thermal environment.

magnetic particles into SMP to prepare an amorphous SMP matrix. Through the inductive heating of Fe_3O_4 particles and the actuation of NdFeB particles, the material could be effectively unlocked and locked; thus, the as-prepared soft robot grippers and deployable/reconfigurable antennas exhibited high application prospects in the field of autonomous soft robots. However, for many shape memory actuators, the prestored strain is irreversibly released under the action of an external stimulus, leading to difficulty in achieving programmable shape recovery.[18,19] Therefore, it is particularly important to develop soft actuators with a driving method that can restore the initial state after fixed deformation and drive with low energy consumption.

In recent years, thermally responsive actuators have attracted increasing interest due to their capability of exhibiting large-volume shape changes and enabling various actuation mechanisms. Such actuators can respond to various heat-generating methods such as joule heating,[20,21] photothermal heating,[22,23] and magnetocaloric effects.[24] However, conventional thermally responsive soft actuators are actuated by the difference in the thermal expansion coefficients of the actuation materials. This driving mechanism is affected by material instability factors and faces many problems such as single shape deformation and large energy consumption. Therefore, it is necessary to further develop fresh materials and original ways to achieve a high driving performance of the actuator. Liquid metal (LM, e.g., EGaIn containing 75% gallium and 25% indium) has great potential in soft robots due to the fluidity, metal conductivity, negligible vapor pressure, and low toxicity.[25] Researchers have recently applied LM to thermally responsive actuators, and the prepared thermally responsive actuators exhibit good thermal actuation performance.[26−28] Wang et al. reported that the LM-based needle-like liquid metal gallium nanoswimmer (LMGNS) could autonomously move forward along the tip direction under the irradiation of a continuous near-infrared laser, and its speed reached to 31.22 μm s^{-1} with a laser intensity of 5 W cm^{-2}.[29] However, LM-based liquid actuators with low energy consumption also required an external continuous energy supply to maintain deformation. Therefore, it is of great significance to give LM-based flexible actuators with multi-response response and recovery ability after plastic deformation.

Here, we report a triple-stimulus-responsive soft actuator with plastically retentive deformation and magnetically programmable recovery. The coupling synergistic effect of thermal shrinkage of CNF/PVA/LM and thermal expansion of MPDMS enables the actuator bends and undergoes plastic deformation under electrothermal and photothermal stimuli and exhibits programmable shape recovery in response to a magnetic field in a thermal environment. The actuator is fabricated by combining a CNF/PVA/LM film with good electrical conductivity and photoresponse properties with a magnetically responsive MPDMS film. Based on the good electrical conductivity of LM, the as-prepared U-shaped actuator can achieve a bending performance of 114° under a low voltage of 1.2 V. Furthermore, the developed actuator exhibits positive noncontact and long-distance actuation performance under NIR light (0.64 W cm^{-2}). With the good multifield coupling energy conversion ability of soft actuators, the successful application of carrier robots and handling robots demonstrates the great potential of actuators in soft robots and smart devices.

RESULTS AND DISCUSSION

Preparation and Characterization of CNF/PVA/LM/MPDMS (CPLMMP) Film. The self-assembly fabrication steps of the CNF/PVA/LM films are shown in Figures 1a and S1. First, the CNF powder is dissolved in deionized (DI) water and stirred to obtain a CNF aqueous solution. Subsequently, a typical LM is dropped into the solution and ultrasonically treated to form a suspension. Then the poly(vinyl alcohol) (PVA) aqueous solution is mixed with the suspension and ultrasonically homogenized. It is worth noting that CNF/PVA/LM suspension maintains its stability even after more than 2 weeks (Figure S3a,b). The CNF serves as a dispersant

https://doi.org/10.1021/acsnano.3c08888
ACS Nano 2023, 17, 24042−24054

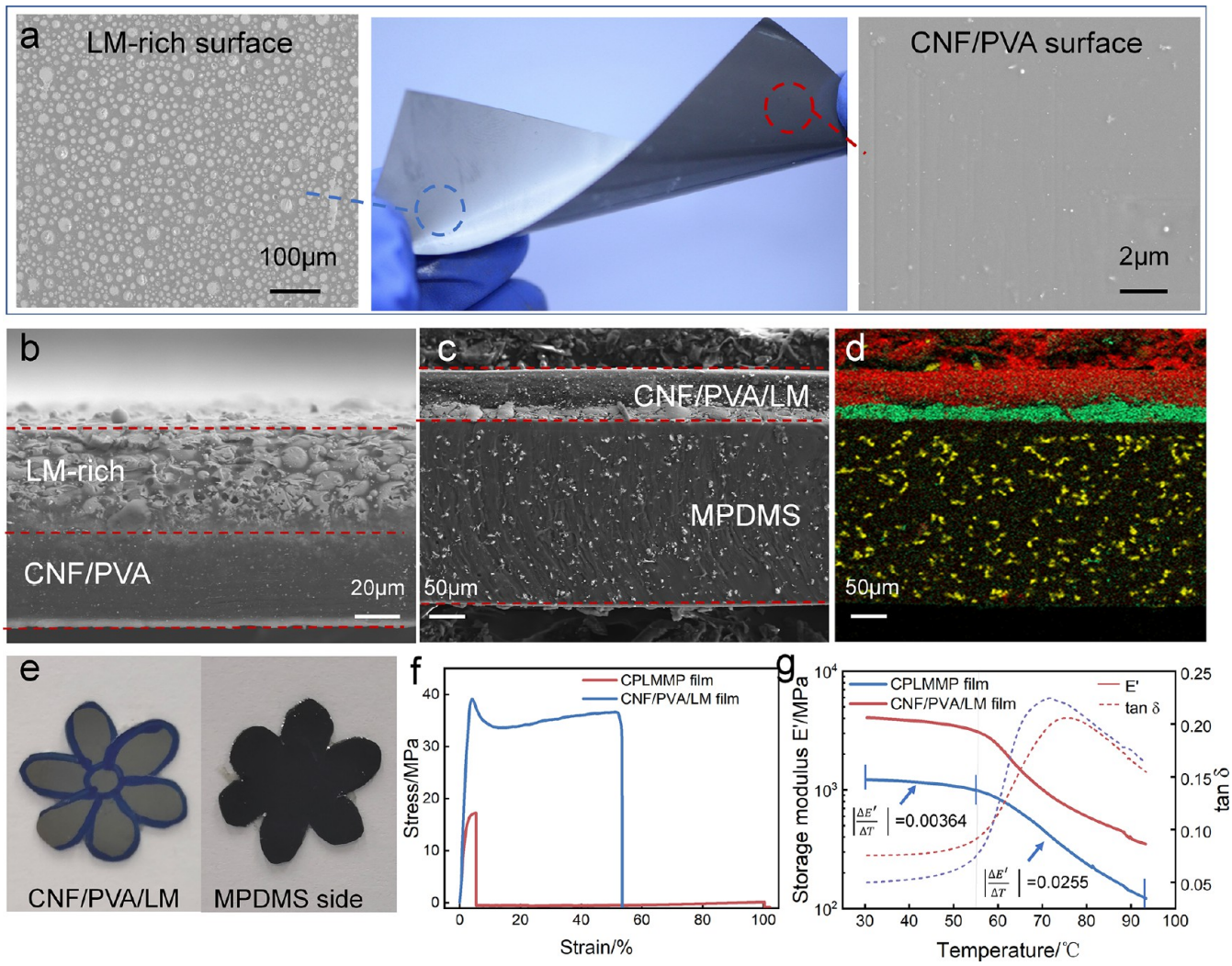

Figure 2. Characterization of the CPLMMP film. (a) Photograph of the CNF/PVA/LM film (middle) and SEM images of its LM-rich and CNF/PVA surface. (b) SEM image of the cross section of CNF/PVA/LM film. (c) SEM image and (d) the corresponding elemental image of the cross section of CPLMMP film. Red is C element, green is In element, and yellow is Fe element. (e) Front and back photos of CPLMMP film in flower shape. (f) The strain−stress curves of CNF/PVA/LM film and CPLMMP film. (g) Curves of the storage modulus of CNF/PVA/LM film and CPLMMP film as a function of temperature.

to stabilize the LM droplets, while the PVA is used as a polymer dispersant and matrix toward a large-area CNF/PVA/LM film with a flat surface. Then the suspension is poured into a poly(methyl methacrylate) (PMMA) mold. After water evaporation, the CNF/PVA/LM film with two different surfaces is formed and peeled off from the substrate. As displayed in Figures 2a and S3c, the CNF/PVA and LM-rich surfaces of the prepared films display different colors due to the difference in composition. The CNF/PVA surface is mainly composed of nanocellulose and the PVA, displaying gray black. The LM-rich surface is mainly composed of LM droplets, exhibiting a silver white. Figure 2b exhibits the cross-sectional SEM image of the CNF/PVA/LM film. LM droplets are mainly distributed at the bottom due to their own gravity and they stacked one by one. In addition, the mapping indicates that elements C and O (as the main components of CNF and PVA) are mainly distributed in the CNF/PVA layer, while elements Ga and In are mainly distributed in the LM-rich layer (Figure S4a).

Figures 1a and S2 present the scheme for the preparation of CNF/PVA/LM/MPDMS(CPLMMP) film. First, the NdFeB/PDMS (MPDMS) solution is spun onto the silicon wafer and peeled off after curing. Then plasma treatment and mechanical pressure are applied to form strong bonding between the MPDMS film and the CNF/PVA/LM film. Finally, the triple-responsive soft CPLMMP film is obtained. The schematic diagram and microscopic cross-section of the CPLMMP composite film (Figures 1b and 2c) demonstrate the CNFs are distributed on the top and the LMs are evenly distributed on the bottom of CNF/PVA/LM film. At the same time, in the magnetized MPDMS film, the magnetic poles of the NdFeB particles point in the same direction. Moreover, Fe is uniformly distributed in the PDMS, while C, Ga, and In are mainly distributed in the upper layer (Figures 2d and S4b) which is consistent with the analysis results of Figure 1c. In the photo of the CPLMMP composite film (Figure 2e), the CNF/PVA/LM side appears gray, and the other side presents black due to the presence of NdFeB particles.

Additionally, the CNF/PVA/LM film can be easily recycled through cutting into pieces and dissolving in DI water, followed by the previous fabricating steps. The CNF/PVA/LM films after recycling 3 times display little difference in

https://doi.org/10.1021/acsnano.3c08888
ACS Nano 2023, 17, 24042−24054

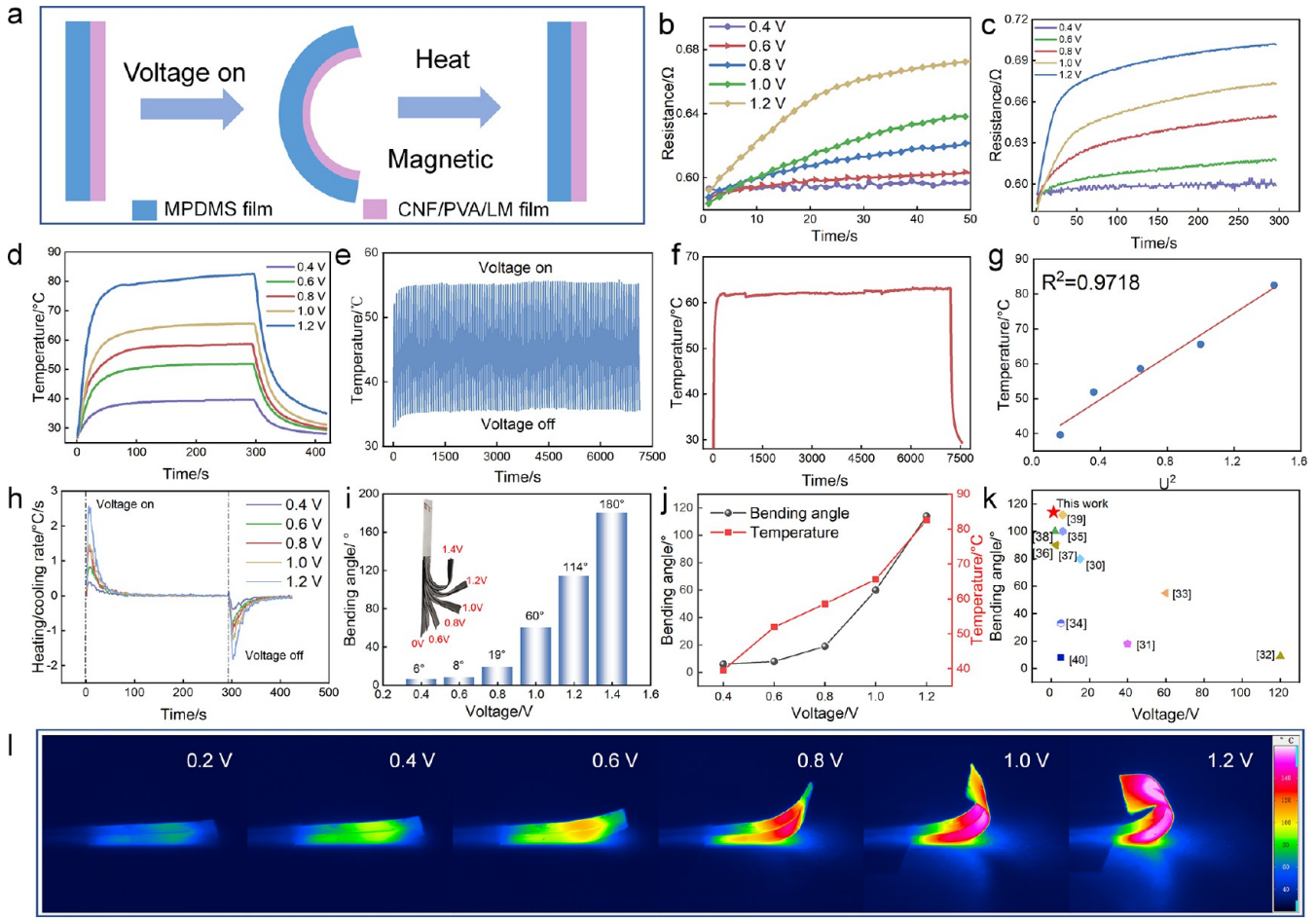

Figure 3. Electrothermal drive performance of the CPLMMP actuator. (a) Schematic diagram of the electrothermal actuator mechanism. (b) Resistance changes of the CPLMMP actuator at different voltages. (c) Resistance changes and (d) time-dependent temperature profiles under different driving voltages for 300 s. (e) Cyclic electrothermal stability of the actuator at 0.8 V voltage. (f) Temperature stability of the CPLMMP actuator at a constant voltage of 1.0 V. (g) Experimental results of the temperature as a function of U^2. (h) The rate of heating and cooling when the actuator is subjected to different voltages. (i) Bending angle as a function of different driving voltages. Insert is optical view of bending curvatures of actuator at different voltages. (j) Maximal bending angle (black solid curve) and maximal temperature (red solid curve) of the CPLMMP actuator as a function of voltage. (k) Comparison of the performance of the present work with previously reported electro-responsive actuators in terms of maximum bending angle and driving voltage.[30−40] (l) IR electrothermal deformation images of the actuator after the voltage was increased from 0.2 to 1.2 V.

photographs (Figure S5a). The tensile curve of the CPLMMP composite film displays two fracture points during the tensile process (Figure 2f). The first point results from the fracture of the CNF/PVA/LM film, and the second point is attributed to the fracture of the MPDMS film. This result is consistent with the experimental phenomenon in the tensile process. The CPLMMP composite film exhibits distinct ferromagnetic properties (Figure S5b) with large remanence and coercive force, which arise from the ferromagnetic NdFeB particles embedded in the PDMS. The magnetization of the sample reaches saturation at ∼1.2 T and the maximum magnetization of the 30 wt % CPLMMP film is 17.88 emu g^{-1}. The CPLMMP actuator can achieve significant bending under a 19 mT magnetic field (Figure S7b), demonstrating a good magnetic driving performance. Figure S5c presents the normalized UV−vis-NIR absorbance of the CNF/PVA surface and LM-rich surface of CNF/PVA/LM film, respectively. The absorption of the LM-rich surface is much greater than that of the CNF/PVA surface. Since the CNF/PVA/LM films possess good absorption of 808 nm infrared light, the temperature of the CPLMMP composite film will increase when NIR light is irradiated, demonstrating a good photothermal effect. Due to the presence of LM in the composite film, the composite film has good conductive properties. As shown in the Figure S6, with an increase of the LM content, the resistance and surface resistivity (Table S1) of the CNF/PVA/LM film decreases and its surface conductivity (Table S2) increases. The resistances of the CNF/PVA/LM films with LM mass fractions of 10, 12.5, and 15 wt % do not change much, but the weights of the films increase, so it is a better choice to choose a LM mass fraction of 10 wt %. In addition, the effect of different ultrasonic time on the conductivity of the CNF/PVA/LM film was also studied. When the ultrasonic time is too long, the ultrasonic droplets of LM become smaller and do not completely settle at the bottom of the film, resulting in a decrease in the conductivity of the film. The short ultrasonic time makes the LM droplets vary in size, but this has little effect on the conductivity of the film. In summary, 60 min is an appropriate ultrasound time. And the resistance of the prepared U-shaped actuator is only 0.2 Ω (Figure S7c). Based on the good conductive properties of the composite

https://doi.org/10.1021/acsnano.3c08888
ACS Nano 2023, 17, 24042−24054

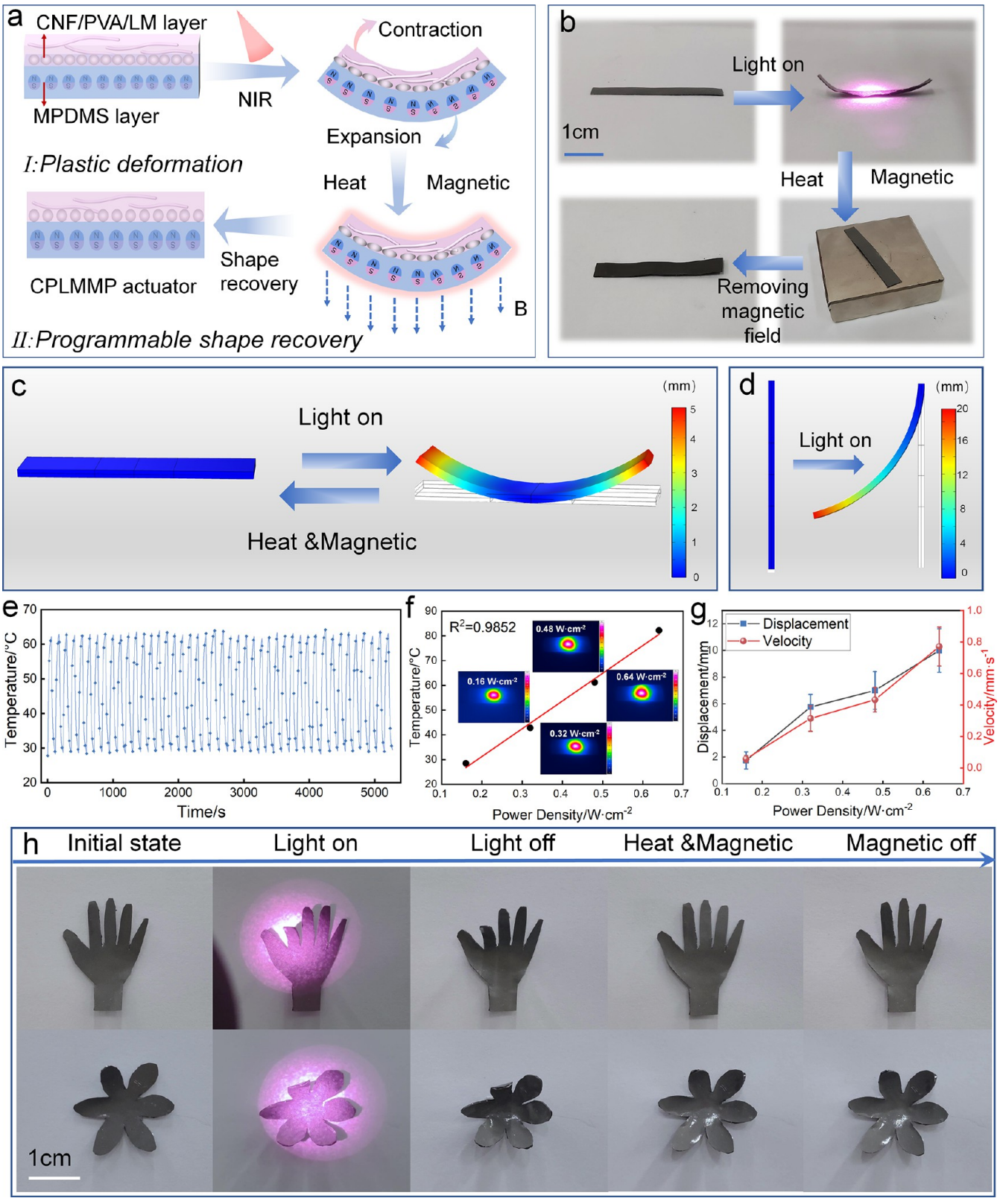

Figure 4. Actuation performance of CPLMMP actuator in NIR light. (a) Schematic diagram and (b) photographs of photothermal deformation and shape recovery under a magnetic field in a thermal environment. (c) Finite element simulation of actuator deformation under NIR light and shape recovery under magnetic/thermal conditions. (d) Finite element simulation of the deformation process of the actuator's tip under NIR light irradiation. (e) Cyclic electrothermal stability of the actuator at 0.48 W cm^{-2} power densities. (f) Infrared power density as a function of temperature. Insets are thermal images with infrared power density. (g) Tip displacement and execution speed at different infrared power densities. (h) Optical images of actuators with hand and flower shapes molded under NIR light and recovered under magnetic/thermal conditions.

https://doi.org/10.1021/acsnano.3c08888
ACS Nano 2023, 17, 24042−24054

film, the actuator exhibits an awesome electrothermal effect when the voltage is applied.

In order to further study the mechanical properties of the composite films, the thermomechanical properties of the composite films were tested. As shown in Figure 2g, the modulus of CNF/PVA/LM film and CPLMMP composite film decreases with the increase of temperature. The CNF/PVA/LM film and CPLMMP composite film exhibit a storage modulus of ∼4 and 1.2 GPa respectively at low temperature (30 °C). As the temperature increases, the modulus of CPLMMP composite film progressively decreases to 0.136 GPa at 90 °C. Before 55 °C, the deformation of the composite film is elastic deformation. As the temperature increases above 55 °C, the CPLMMP composite film undergoes plastic deformation. Therefore, the CPLMMP composite film exists potential applications in electrothermal, photothermal, and magnetic coupling drives (Figure 1b).

Electrothermal Drive Properties of the Flexible CPLMMP Actuator. Based on the favorable electrical conductivity of LM and the difference in thermal expansion coefficients of the CNF/PVA/LM film and MPDMS film, the CPLMMP actuator exhibits ideal electrothermal driving performance. In order to prove the electrothermal driving performance of the CPLMMP film, the CNF/PVA/LM film was cut into a U-shape and the circuit was brushed out on the LM-surface with a brush. Finally, the U-shaped actuator was prepared by compounding the CNF/PVA/LM film with the MPDMS film. The photos and dimensions of the U-shaped actuator are exhibited in Figure S8a. When the actuator is electrically stimulated, the LM converts the electrical energy to heat. Due to the different coefficient of thermal expansion between MPDMS layer (203.7×10^{-6} k^{-1}) and CNF/PVA/LM layer (-454.5×10^{-6} k^{-1}), the MPDMS layer expands while the CNF/PVA/LM layer shrinks when the actuator is powered on. Under the action of two-layer expansion-contraction coupling, the actuator is bent by being transferred from a flat state to a curved state (Figure 3a). Different from the previously reported elastic actuator, the CPLMMP actuator can hold the bending angle after turn off the power. Because when the power is stopped, the temperature of the actuator decreases, the plastic deformation of the actuator allows it to maintain its shape. However, the modulus of the actuator is very low in the thermal environment of 80 °C, the actuator can be restored to the original plane state when the film is cooled again under the attraction of the magnetic field.

During the bending process, the resistance of the actuator exhibits good stability. When the applied voltage increases from 0.4 to 1.2 V (Figure 3b) and is energized for 300 s (Figure 3c), the resistance of the actuator is basically unchanged. Figure 3d displays the time−temperature correlation curves of the actuators under different voltages. When a voltage is applied to the actuator, the actuator temperature rises rapidly until its heat production equals its heat loss, thus reaching the saturation temperature. When the voltage is removed, the actuator temperature quickly drops to room temperature. Besides, cycle stability of the actuator's electrothermal performance was also investigated by fixing both ends of the actuator (Figure 3e). For each cycle, by applying and removing applied voltages within 75 s, the temperature rises to the saturation temperature and then drops to the initial temperature. After 100 heating−cooling cycles, the CPLMMP actuator still maintains its saturation temperature of around 55 °C at a 0.8 V applied voltage. Furthermore, the temperature change over a long time at a constant voltage of 1.0 V is recorded to evaluate the long-term heating stability of the CPLMMP actuator (Figure 3f). It is observed (Figure 3g) that the saturation temperature increases monotonically as the applied voltage increases. In the first 9 s after turning on the power, the heating rate (i.e., the rate of temperature increase) is the highest. However, when the temperature achieves a certain high level, the large heat loss results in a lower heating rate, as displayed in the heating cycle of Figure 3h.

The maximum bending angle of the actuator increases with the increase of applied voltage (Figure 3i) and the illustration displays photographs of bending angles at different voltages. Higher driving voltages lead to higher temperatures and greater actuator deformation (Figure 3j), indicating that the temperature is one of the main factors in actuator bending deformation. When the drive voltage is increased to 1.2 V, the actuator temperature reaches 82.5 °C and the bending angle reaches 114°. The definition of the bending angle is shown in Figure S8b. The infrared electrothermal deformation image of the actuator in Figure 3l shows that the color of the actuator changes from blue to red as the applied voltage increases, corresponding to the rise in temperature and bending angle. In comparison to the previously reported electrothermal actuators, our actuators exhibit satisfactory actuation performance (Figure 3k). Two key parameters (bending angle and driving voltage) were used to compare the driving ability of CPLMMP actuators. It is noted that the CPLMMP actuator reported in this work has a larger bending angle (114°) at a lower driving voltage (1.2 V) than most of the previously reported actuators based on the electrothermal mechanism. Therefore, this method provides an advanced idea for the preparation of low-energy electrothermal soft actuators.

Photothermal Drive Performance of the Soft CPLMMP Actuator. Interestingly, the actuator can also be stimulated by applying NIR light. As shown in the Figure 4a and b, under NIR light irradiation, the CNF/PVA/LM layer shrinks and the MPDMS layer expands, causing the MPDMS layer to bend toward the CNF/PVA/LM layer of the actuator. After removing the NIR light, the plastic deformation of CPLMMP actuator cannot be recovered, and the shape of the actuator is fixed. However, similar to the electrothermal actuation process, the actuator shape can be programmable recovered by magnetic attraction in the thermal environment. For the deformed CPLMMP actuator, if it is placed in a thermal environment, the actuator can recover its original shape under the action of an external magnetic field due to the reverse deformation acted by magnetic forces on the MPDMS. As previously described, the modulus of the composite film changes dramatically at 55 °C. Above 55 °C, the actuator undergoes plastic deformation by external stimulation. Below 55 °C, the composite film is in the elastic deformation stage, and the high modulus and dead weight limit the deformation of the actuator. By alternating the temperature between these two states, the actuator can deform at $T > 55$ °C and transform into the desired shape by turning on NIR light, and then locks its shape at $T < 55$ °C (turning off NIR light). When the shape of the actuator is locked, the actuator keeps its shape without any energy input to hold the payload, thus exhibiting a shape-memory behavior that can be exploited for soft gripping applications.

In order to further study and verify the photothermal driving mechanism of the CPLMMP actuator, the deformation characteristics of the strip CPLMMP actuator were simulated

https://doi.org/10.1021/acsnano.3c08888
ACS Nano 2023, 17, 24042−24054

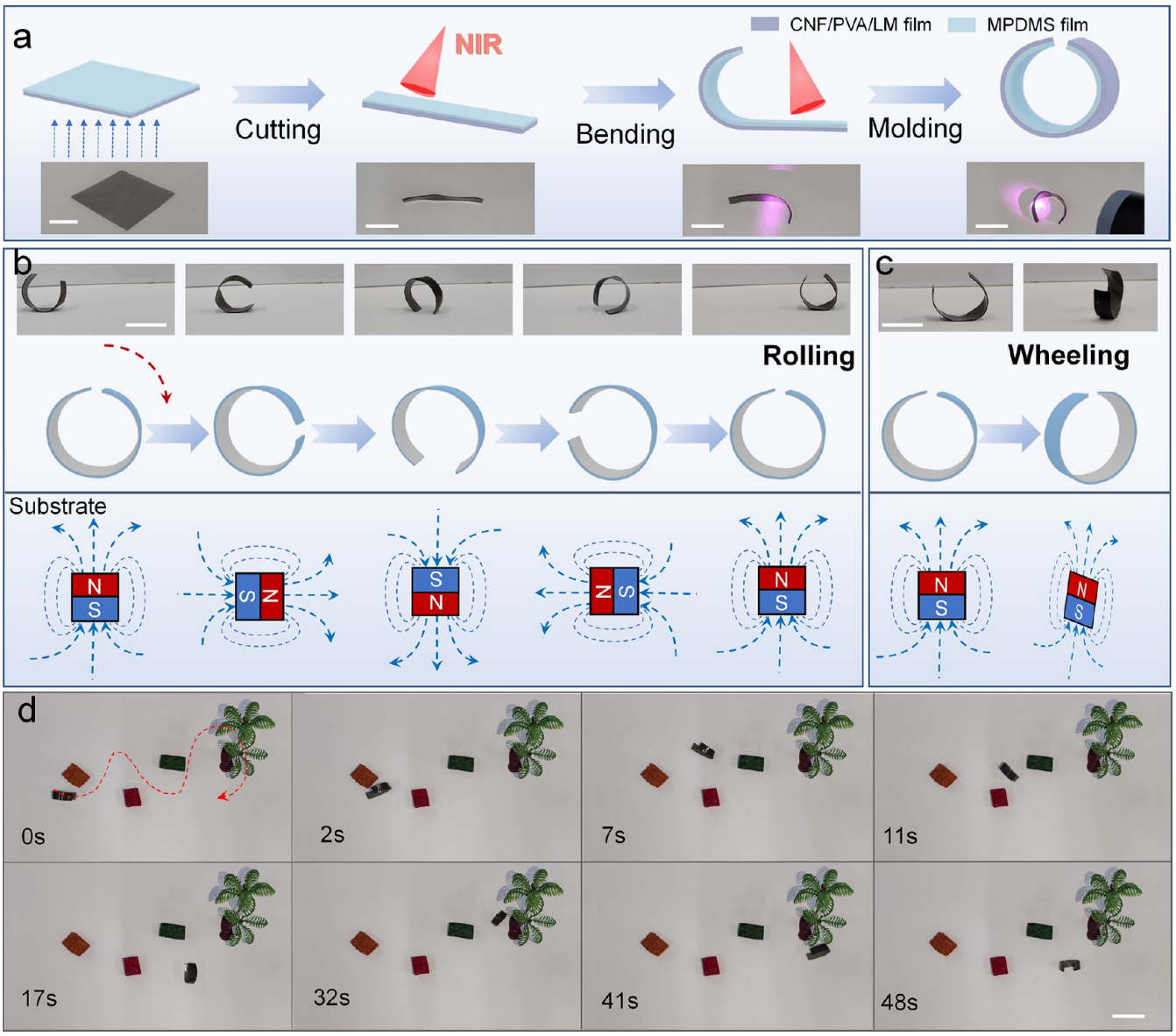

Figure 5. (a) The preparation diagram of the rolling robot. (b) Schematic diagram and optical photograph of linear motion of a rolling robot as the direction of magnetic field changes. (c) Schematic diagram and optical photograph of a rolling robot changing direction as the magnetic field direction changes. (d) Physical image of a rolling robot following a magnetic field to avoid obstacles. Scar bar: 2 cm.

by using the finite element method (FEM) (Figure 4c,d). The geometric model designed by SolidWorks software was imported into COMSOL. In the simulation of the noncontact photothermal actuator, the three physical fields of optical field, thermal field, and solid mechanics are used as the coupling solution in the finite element, and the research type is steady state. For the open strip actuator, when the light source irradiates the middle part of the actuator, both ends of the actuator begin to bend (Figure 4c), while for the strip actuator fixed at one end, only unilateral bending occurs, and the bending mainly appears in the light source irradiation part (Figure 4d). The simulation results of the strip actuator under NIR light are consistent with the experimental results as presented in Figure S9a and Video S1.

When NIR light is irradiated in the middle of the strip actuator, the photothermal effect of LM will heat the CNF/PVA/LM layer and achieve driving behavior in response to light. To further explore the photothermal properties of CPLMMP actuator, four kinds of NIR light with different powers were used to irradiate the composite film (Figure S9b) and the temperature change during the whole process was recorded by an infrared thermal imager (Figure 4f). The results manifest that with the increase of light power the temperature of the actuator is obviously enhanced. The photothermal performance of the actuator depends on the light intensity of NIR light and a larger bending displacement and larger velocity can be produced by higher power density of NIR light (Figure 4g). Moreover, switching off the NIR light led to rapid cooling of the actuator due to the large differences between the temperature of actuator and the room temperature. After 100 times repeated NIR light irradiation, the actuator is found to possess satisfactory photothermal stability, which guarantees subsequent experiments of the actuator (Figure 4e).

As shown in Figure S10a, after being stimulated by NIR light (0.64 W cm^{-2}), one end of the strip actuator is bent from an initial angle of 6° to 44°. Then a magnet is added below the

https://doi.org/10.1021/acsnano.3c08888
ACS Nano 2023, 17, 24042−24054

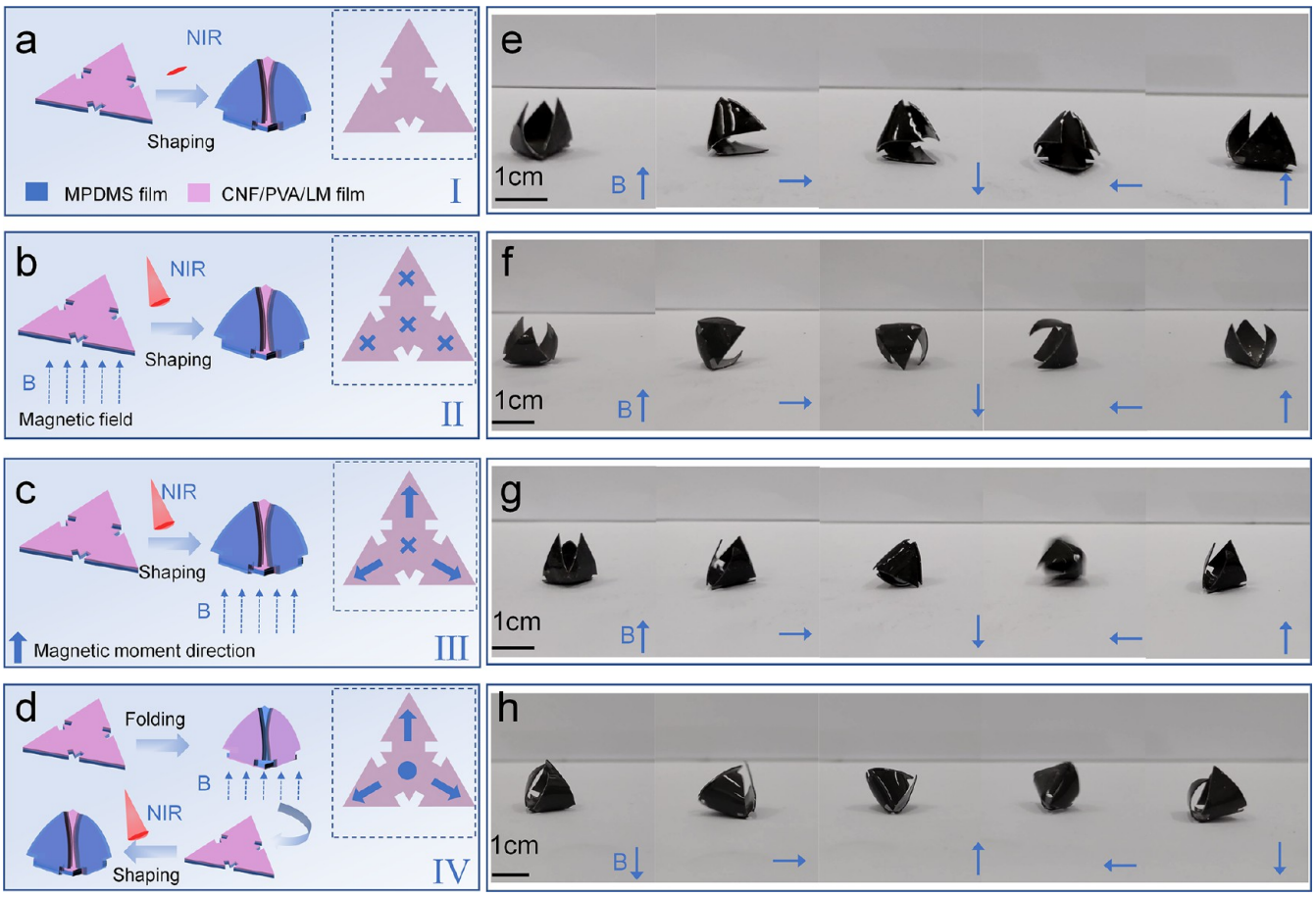

Figure 6. (a–d) Preparation schematic diagram of four different modes (I–IV) of magnetization for carrier robots. (e–h) Optical photographs of four kinds of carrier robots following a magnetic field for one cycle without loading.

actuator and the strip actuator is attracted by the magnetic field to deform at an angle of 0° under heating. Finally, the strip actuator returns to its original angle after removing the magnetic field. The results of 25 cycles of experiments have proven that the actuator has good durability and long-term stability (Figure S10b). The deformation and recovery process of actuators in the shape of hands and flowers are displayed in Figure 4h. When the response part of the actuator is illuminated by NIR light, deformation occurs under the action of photothermal effect. Subsequently, the NIR light is turned off and the actuator shape is fixed. After heating it in an oven (80 °C) for 3 min, and then placing it on a magnet, the responsive part of the actuator is recovered to its original state, demonstrating its potential application in complex environments. In addition, under the stimulation of NIR light, the designed braille letters "I," "M", "V", and "C" deform and bulge at fixed points and then recover under the attraction of a magnetic field, successfully realizing a contactable and refreshable braille array (Figure S11).

Based on the programmability of the CPLMMP actuator, the strip actuator can be assembled as a rolling robot, demonstrating the ability to avoid obstacles and continue moving forward in complex environments (Figure 5). The preparation method of the rolling robot is shown in Figure 5a. First, a strip is cut on the film with a size of 4 × 0.5 cm^2, and then one end of the strip is irradiated with NIR light until it bends to 90°. Finally, the other end is also irradiated with NIR light until the strip turns into a circle. The rolling robot can either roll as the magnet poles change, or change direction as the magnet changes direction. Due to the ferromagnetic properties of NdFeB (high remanence), the innovative moment will be conserved when the external field is removed, thus resulting in programmable magnetization profiles.[41] For example, the rolling robot will be attracted when a reverse magnetic pole (≈ 200 mT) is placed at the bottom of the rolling robot. When the magnetic poles rotate, the rolling robot also rotates to align its own torque with the magnetic field below the substrate (Figure 5b,c).

Through the repeated process of attraction and repulsion, the rolling robot achieves a rolling motion. In nature, reptiles have the ability to avoid obstacles, which is a challenge for traditional soft robots, while our rolling robots have advantages in rolling and avoiding obstacles in complex geographical environments. Figure 5d exhibits the obstacle avoidance ability of rolling robots. The speed of the roller can be adjusted by rotating the magnet under the substrate. The rolling robot passes through a road with four obstacles at a speed of ~0.66 cm/s (Figure 5d). More importantly, the rolling robot can return to its original shape under the attraction of magnets in a hot environment, which has gratifying recyclability (Figure S12). The flexible adjustment of the rolling robot's straight and turning during the journey demonstrates its broad application prospects in complex environments.

In addition to the rolling robot, the carrier robot also displays the programmable shape recovery characteristics of the CPLMMP actuator. Based on the origami magnetization

https://doi.org/10.1021/acsnano.3c08888
ACS Nano 2023, 17, 24042–24054

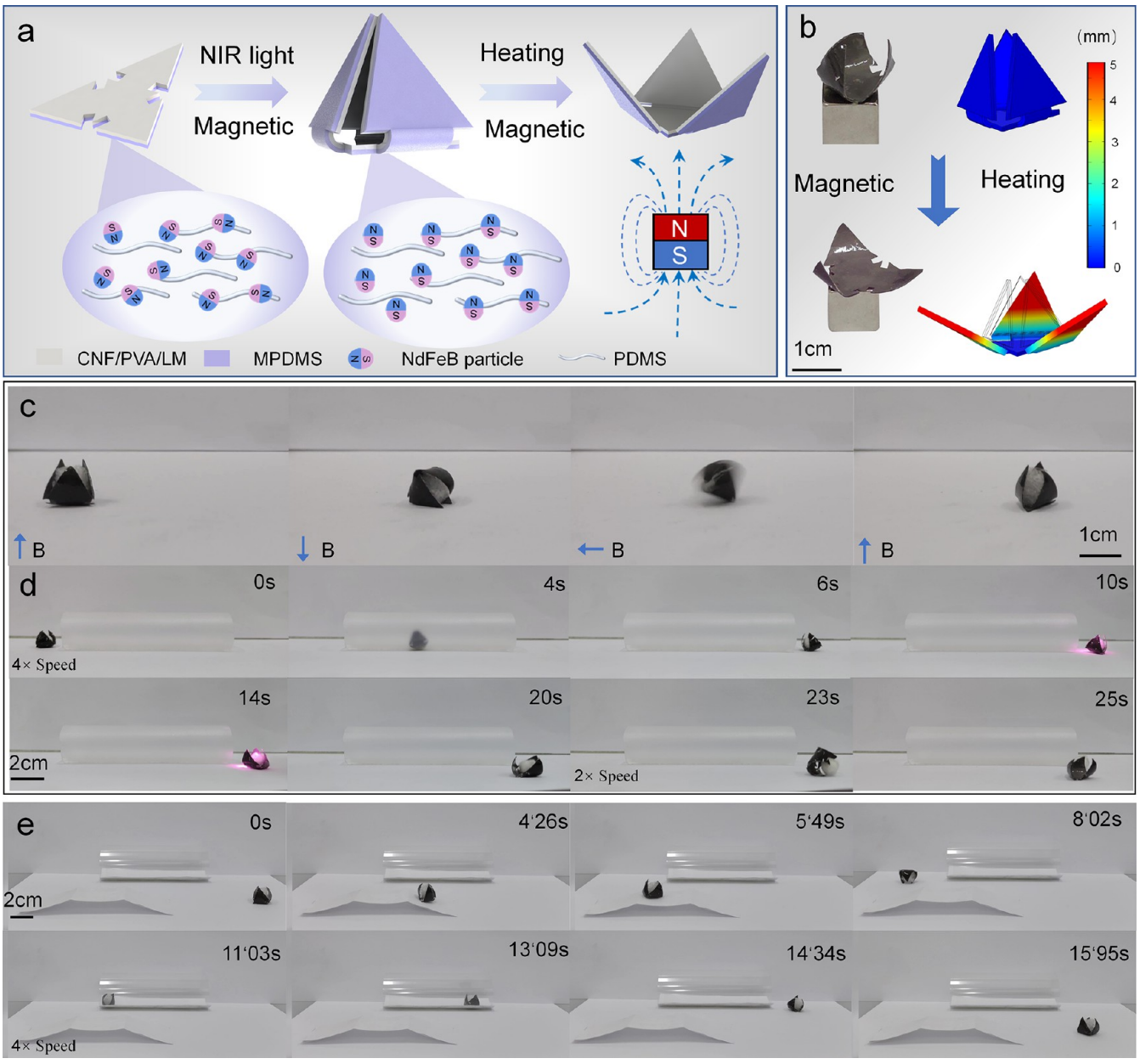

Figure 7. (a) Schematic diagram of photothermal deformation and thermal/magnetic recovery of a carrier robot. (b) Three limbs of a carrier robot released under magnetic attraction in a thermal environment. The illustration is the result of finite element simulation of magnetic release process. (c) The carrier robot is wrapped in an optical picture of an object moving in a magnetic field for one cycle. (d) Process optical image of a carrier robot wrapping an object through a frosted pipe and releasing the object at a fixed point. (e) A demonstration of a carrier robot wrapping an object through a 30° ramp and through a transparent pipe.

strategy, the composite film was fabricated into a regular triangle carrier robot by the cutting method. In considering of the programmable magnetization properties of NdFeB particles, four different magnetization methods are used to prepare a carrier robot with different combinations of magnetization directions (Figure 6).

The first one (I) is that the three limbs of the composite film are deformed and gathered together to form a pyramid shaped carrier robot under NIR light (0.64 W cm^{-2}) (Figure 6a). Due to the unmagnetized NdFeB possessing soft magnetic properties, the soft robots are attracted and dragged forward (Figure 6e) when the magnet under the substrate rotates and the magnetic field changes. As shown in Figure 6b, the second (II) is a planar magnetized carrier robot that places the composite film in a 1.5 T magnetic field. The M of the magnetized film is presented in the inset schematic diagram, and the arrow indicates the internal magnetization direction. Then the magnetized composite film is irradiated with NIR light, and the shape of the carrier robot is fixed after removing the NIR light. The magnetization direction of the center of the plane magnetized carrier robot is consistent with that of the surrounding three limbs, so when attracted by the magnetic field under the substrate, the converged three arms will be slightly released. When the magnetic field below changes, the carrier robot will undergo a rotation process of attraction and repulsion attraction (Figure 6f). Due to the mutual repulsion of the three limb magnetic poles, they sometimes eject the

https://doi.org/10.1021/acsnano.3c08888
ACS Nano 2023, 17, 24042−24054

goods in the process of carrying goods, which possess poor stability.

The third (III) is the forward magnetization carrier robot (Figure 6c). First, the carrier robot is shaped under NIR light, and then the pyramid shaped soft robot is placed in a (1.5 T) magnetic field for magnetization. Thus, the carrier robot with different magnetization directions between the center and the three surrounding limbs can be obtained. When the magnetic field under the substrate changes, one limb *M* of the carrier robot forms an included angle with the direction of the magnetic field under the deflection of the magnetic field, so the robot rolls under the action of torque, and finally completes the rolling motion cycle (Figure 6g). The carrier robot prepared by this method exhibits transfer and fixed-point release functions. The last (IV) is the reverse magnetization robot, in which the composite film was first folded into a pyramid shape and fixed with tape, then put into a (1.5 T) magnetic field for magnetization, and finally the magnetic field and the tape were removed and then shaped with NIR light (Figure 6d). In this carrier robot, the center is opposite to the magnetic pole of the third carrier robot. When the magnetic field under the substrate changes, the limb M of the handling robot forms an angle with the direction of the magnetic field under the deflection of the magnetic field so that the robot moves under the action of the torque and finally completes the handling task (Figure 6h). In order to compare the shape fixing ability of CPLMMP carrier robots (III) after plastic deformation, carrier robots with the same magnetic field distribution based on MPDMS film were prepared. As shown in Figure S15 and Video S3, the planar carrier robot turns into a triangular pyramid shape driven by the *Y*-axis magnetic field and then moves forward under the guidance of the Y−Z rotating magnetic field provided by the 3D magnetic field. After one cycle, the magnetic field is removed and the carrier robot returns to a planar shape. However, the carrier robot prepared based on the CPLMMP composite film maintains its shape without changing in the Y−Z rotating magnetic field provided by the 3D magnetic field (Figure S16 and Video S4). Based on the desirable shape fixing ability, the CPLMMP delivery robot can well face complex environments even when wrapping objects.

By adjusting the magnetic field, the carrier robot can be remotely operated. In order to better understand the motion mechanism of the carrier robot, the third carrier robot (III) (Figure 6c) is chosen to study the transport performance. The dimensional diagram of the photos before and after deformation of the carrier robot is displayed in Figure S13a,b. Figure 7a displays the process of retracting and releasing the three limbs of the carrier robot. After being heated, the moduli of the three limbs of the carrier robot decrease. Under the attraction of the edge magnetic field of a 1 × 1 × 1 cm^3 magnet, the three limbs that converge bend outward, thereby the object was released (Video S5). The simulation results of the release process of the carrier robot under a magnetic field are shown in Figures 7b, S13c, and S14. Appropriate plastic deformation and shape recovery under magnetic-field-thermal attraction capabilities enable the CPLMMP carrier robot to move forward in complex environments and release objects at the target location.

As exhibited from the photographs of robot locomotion, the carrier robot rotates for one revolution when the rotating magnetic field operates for one cycle. Consequently, the speed of the rolling motion of the carrier robot is closely related to the rotational frequency of the rotating magnetic field. Driven by magnetic force, the carrier robot wrapped around the cargo achieved a rotational motion within 3 s, demonstrating good transport speed (Figure 7c). Figure 7d and Video S6 illustrate the carrier robot carrying goods, smoothly passing through a frosted pipeline under a rotating magnetic field and achieving the release of goods under the control of NIR and magnetic field at the edge of the magnet. Compared with the movement of objects wrapped by a carrier robot in the Y−Z rotating magnetic field provided by the 3D magnetic field (Figure S17 and Video S7), it is more convenient to use small magnets to control the movement of the carrier robot to release the object at the target location. In addition, the carrier robot can carry goods and smoothly pass through a 30° slope according to the target trajectory and then pass through a flat straight surface and pipeline until it reaches the destination, with no loss of goods in the picture (Figure 7e and Video S8). Note that the carrier robot can perform rolling and crawling motions in different topographical conditions, including frosted pipelines, paper surfaces, and slopes, without losing its precise controllability. This simple and good photothermal plastic thermal magnetic recovery feature greatly expands the application field of soft actuators.

CONCLUSION

In summary, a soft actuator composed of a combination of CNF/PVA/LM films with good electrical conductivity and magnetic PDMS was designed and fabricated and possesses electric-NIR-magnetic triple-response performance. The CNF/PVA/LM layer of the actuator contracts under electrothermal or NIR light stimulation, while the MPDMS layer expands, resulting in bending deformation of the CPLMMP actuator. After the stimulus is removed, the shape of the actuator is fixed. Finally, programmable shape recovery of the actuator is achieved by applying a magnetic field in a thermal environment. More importantly, the soft actuator can achieve large bending (114°) at a low voltage (1.2 V) and long-distance actuation is possible under low-intensity NIR light (0.64 W cm^{-2}). Through changing the direction of the simple magnetic field, the obstacle avoidance ability of the rolling robot and the complex continuous motion of the carrying robot are demonstrated. This study develops an actuation strategy integrated with multistimuli response, remote control, lower driving voltage, and programmable complex deformation, which will provide high potential in exploring smart materials for complex biomimetic systems.

METHODS

Materials. The CNF powder was purchased from Qihong Co., Ltd., China. Poly(vinyl alcohol) powder (PVA-1799) was purchased from Aladdin Inc. The liquid metal (75% gallium, 25% indium) with a melting point of 16 °C was purchased from Yongcheng Co., Ltd., China. NdFeB powders were purchased from Guangzhou Nord Transmission Co., Ltd., with an average particle size of 5 μm. The polydimethylsiloxane (PDMS) precursor and curing agent (Sylgard 184) were purchased from Dow Corning. All of the above chemical reagents were employed without further purification, and distilled water was used.

Preparation of CNF/PVA/LM Film. CNF powder (0.1 g) was dissolved in 10 mL of DI water and stirred with a glass rod for 20 min at room temperature. The 1.91 g of LM was dropped into the CNF solution and dispersed with an ultrasonic disruption system for 60 min. PVA powder (5 g) was mixed with 60 mL of DI water, and then the solution was stirred for 1 h at 100 °C. Subsequently, 8 mL of PVA

https://doi.org/10.1021/acsnano.3c08888
ACS Nano 2023, 17, 24042−24054

solution was poured into the CNF/LM suspension and ultrasounded for 20 min to obtain a uniform mixed suspension. The prepared suspension was cast in a PMMA mold at room temperature for 24 h to be dried. The CNF/PVA/LM film was obtained after the complete evaporation of water.

Fabrication of the CNF/PVA/LM/MPDMS Film and Photothermal Response Actuator. First, MPDMS magnetic films were synthesized by the spin-coating process. NdFeB powder (30 wt %), PDMS and cross-linking agent (10:1) were added into a three-mouth flask and stirred at a speed of 600 rpm for 30 min. Then 3 mL of PDMS/NdFeB (MPDMS) mixture was poured on a silicon wafer for spin-coating and cured at 90 °C. The obtained MPDMS film was quickly coated with a layer of ultrathin PDMS solution after plasma treatment, then affixed with CNF/PVA/LM film, and placed on the 90 °C heating plate for curing. Finally, the CNF/PVA/LM/MPDMS film with a photothermal response was obtained. The CPLMMP film is designed into the shapes required for the experiment (such as hand, flower, strip, and triangle), and then cut with an art knife to obtain a variety of shapes of photothermal response actuators.

Fabrication of the Electrothermal Response CNF/PVA/LM/MPDMS Actuator. First, the LM-rich side of the CNF/PVA/LM film was brushed out of the U-shape circuit through the PET mask plate, and then, it was bonded with the MPDMS film after plasma treatment through the PDMS solution. Finally, the composite film was placed on a heating Table (90 °C) and pressed by the printed plastic block. After curing for 15 min, the electrothermal response actuator was obtained.

Characterization. The morphologies of CNF/PVA/LM film and CNF/PVA/LM/MPDMS film were characterized by an SEM Gemini 500 (Carl Zeiss Jena, Germany) equipped with an energy-dispersive spectroscopy (EDS) system. The mechanical properties of the CNF/PVA/LM film and CNF/PVA/LM/MPDMS film were tested by the Materials Test System (MTS). Electrical properties were measured using ModuLab test system (Solartron Analytical, AMETEK Advanced Measurement Technology, Inc.) with a sweep voltage from −40 to 40 mV. The electrothermal performance of CNF/PVA/LM/MPDMS actuator was explored by an auto range DC power supply (IT8500, Itech electronic Co., Ltd.) and a thermocouple device (DT-3891G, Shenzhen Everbest Machinery Industry Co., Ltd., China) with a multiple datalogger data analysis software. Infrared electrothermal images were recorded with an infrared camera (ImageIR 8325). The hysteresis loops of the materials were tested by HyMDC (Hysteresis Measurement of Soft and Hard Magnetic Materials). The thermomechanical properties were measured by a dynamic mechanical analysis (DMA Q800). The test temperature was raised from 25 to 95 °C by 10 °C min^{-1}.

The electrical conductivity of the CNF/PVA/LM film is calculated by the formula:

$$\sigma = \frac{1}{\rho} = \frac{L}{R \times S}$$

where σ is the surface conductivity of the CNF/PVA/LM film, ρ is the surface resistivity of the CNF/PVA/LM film, R is the measured resistance of the CNF/PVA/LM film, L is the effective length when measuring the resistance of CNF/PVA/LM film, and S is the effective area when measuring the resistance of CNF/PVA/LM film.

ASSOCIATED CONTENT

Supporting Information

The Supporting Information is available free of charge at https://pubs.acs.org/doi/10.1021/acsnano.3c08888.

Deformation process of strip actuator under NIR light (MP4)

Process of rolling robot avoiding obstacles under guidance of magnetic field (MP4)

Motion process of MPDMS carrier robot under 3D magnetic field (MP4)

No-load motion process of CPLMMP carrier robot under 3D magnetic field (MP4)

Process of deformation and shape recovery of carrier robot (MP4)

Process optical image of a carrier robot wrapping an object through frosted pipe and releasing the object at a fixed point (MP4)

Motion process of CPLMMP carrier robot wrapping objects under 3D magnetic field (MP4)

Demonstration of carrier robot wrapping an object through a 30° ramp and through a transparent pipe (MP4)

Schematic diagram of fabrication process of CNF/PVA/LM film and CPLMMP film; comparation of stability between CNF/PVA/LM and CNF/LM solutions; elemental image of the cross section of CNF/PVA/LM film and CPLMMP film; recyclability photos and UV−vis-NIR absorbance of CNF/PVA/LM film; hysteresis loops and magnetic drive demonstration of CPLMMP films; $I-V$ curves of CNF/PVA/LM films with different LM mass fractions and ultrasonic times; dimension diagram and drive deformation angle definition of U-shaped CPLMMP actuator; bending deformation photos of strip driver; cyclic stability of photothermal deformation and shape recovery under magnetic/thermal conditions; dimensional diagram, deformation process and deformation recovery process of carrying robot; motion process of MPDMS carrier robot and CPLMMP carrier robot under Y−Z rotating magnetic field generated by 3D magnetic field; electrical resistivity and electrical conductivity of CNF/PVA/LM films with LM mass fractions of 5, 7.5, 10, 12.5, and 15 wt % and ultrasonic times of 30, 60, and 90 min (PDF)

AUTHOR INFORMATION

Corresponding Authors

Guojiang Liao − *Science and Technology on Reactor System Design Technology Laboratory, Nuclear Power Institute of China, Chengdu, Sichuan 610213, PR China*; Phone: 86-028-85900378; Email: liao_work@163.com

Xinglong Gong − *CAS Key Laboratory of Mechanical Behavior and Design of Materials, Department of Modern Mechanics, University of Science and Technology of China, Hefei, Anhui 230027, PR China; State Key Laboratory of Fire Science, University of Science and Technology of China, Hefei, Anhui 230026, PR China*; orcid.org/0000-0001-6997-9526; Phone: 86-551-63606382; Email: gongxl@ustc.edu.cn; Fax: 86-551-63600419

Shouhu Xuan − *CAS Key Laboratory of Mechanical Behavior and Design of Materials, Department of Modern Mechanics, University of Science and Technology of China, Hefei, Anhui 230027, PR China; State Key Laboratory of Fire Science, University of Science and Technology of China, Hefei, Anhui 230026, PR China*; orcid.org/0000-0002-8232-9736; Phone: 86-551-63606382; Email: xuansh@ustc.edu.cn; Fax: 86-551-63600419

Authors

Wenwen Li − *CAS Key Laboratory of Mechanical Behavior and Design of Materials, Department of Modern Mechanics, University of Science and Technology of China, Hefei, Anhui 230027, PR China*

https://doi.org/10.1021/acsnano.3c08888
ACS Nano 2023, 17, 24042−24054

Min Sang − *CAS Key Laboratory of Mechanical Behavior and Design of Materials, Department of Modern Mechanics, University of Science and Technology of China, Hefei, Anhui 230027, PR China*

Congcong Lou − *CAS Key Laboratory of Mechanical Behavior and Design of Materials, Department of Modern Mechanics, University of Science and Technology of China, Hefei, Anhui 230027, PR China*

Shuai Liu − *CAS Key Laboratory of Mechanical Behavior and Design of Materials, Department of Modern Mechanics, University of Science and Technology of China, Hefei, Anhui 230027, PR China*

Jianpeng Wu − *CAS Key Laboratory of Mechanical Behavior and Design of Materials, Department of Modern Mechanics, University of Science and Technology of China, Hefei, Anhui 230027, PR China*

Qian Ma − *BASF Advanced Chemicals Co., Ltd., Shanghai 200137, PR China*

Complete contact information is available at: https://pubs.acs.org/10.1021/acsnano.3c08888

Author Contributions

¶Wenwen Li and Min Sang contributed equally to this work.

Notes

The authors declare no competing financial interest.

ACKNOWLEDGMENTS

Financial support from the National Natural Science Foundation of China (Grant Nos. 12072338, 12132016, 12202435, 52321003), the Anhui's Key R&D Program of China (202104a05020009), the Aviation Science Foundation of China (20200029079004), and the Fundamental Research Funds for the Central Universities (WK2480000007) are gratefully acknowledged. The USTC Center for Micro- and Nanoscale Research and Fabrication also contributed to microstructural characterization.

REFERENCES

(1) Kim, Y.; Genevriere, E.; Harker, P.; Choe, J.; Balicki, M.; Regenhardt, R. W.; Vranic, J. E.; Dmytriw, A. A.; Patel, A. B.; Zhao, X. H. Telerobotic neurovascular interventions with magnetic manipulation. *Sci. Robot.* **2022**, *7* (65), No. eabg9907.

(2) Yang, M. Y.; Xu, Y. Y.; Zhang, X.; Bisoyi, H. K.; Xue, P.; Yang, Y. Z.; Yang, X.; Valenzuela, C.; Chen, Y. H.; Wang, L.; et al. Bioinspired phototropic MXene-reinforced soft tubular actuators for omnidirectional light-tracking and adaptive photovoltaics. *Adv. Funct. Mater.* **2022**, *32* (26), No. 2201884.

(3) Zhao, Y. S.; Lo, C. Y.; Ruan, L. C.; Pi, C. H.; Kim, C.; Alsaid, Y.; Frenkel, I.; Rico, R.; Tsao, T. C.; He, X. M. Somatosensory actuator based on stretchable conductive photothermally responsive hydrogel. *Sci. Robot.* **2021**, *6* (53), No. eabd5483.

(4) Acome, E.; Mitchell, S. K.; Morrissey, T. G.; Emmett, M. B.; Benjamin, C.; King, M.; Radakovitz, M.; Keplinger, C. Hydraulically amplified self-healing electrostatic actuators with muscle-like performance. *Science* **2018**, *359* (6371), 61−65.

(5) Rahman, S.; Wu, L.; El Elmi, A.; Pasini, D. Zero-power shape retention in soft pneumatic actuators with extensional and bending multistability. *Adv. Funct. Mater.* **2023**, No. 2304151.

(6) Saadli, M.; Braunmiller, D. L.; Mourran, A.; Crassous, J. J. Thermally and magnetically programmable hydrogel microactuators. *Small* **2023**, *19* (16), No. 2207035.

(7) Qian, N. N.; Bisoyi, H. K.; Wang, M.; Huang, S.; Liu, Z. C.; Chen, X. M.; Hu, J.; Yang, H.; Li, Q. A visible and near-Infrared light-fueled omnidirectional twist-bend crawling robot. *Adv. Funct. Mater.* **2023**, *33* (16), No. 2214205.

(8) Wang, Y. Q.; Zhu, Y.; Zhang, X. H.; Zhu, F. B.; Qin, Y. X.; Chen, W. Y.; Zheng, Q. Luminescent composite organohydrogels with Fe^{3+}, pH, and glucose-dependent shape memory behavior accompanied with diverse fluorescence variation. *Chem. Eng. J.* **2022**, *450*, No. 137930.

(9) Gao, J. S.; Zhao, X. X.; Wen, J. P.; Hu, D. T.; Li, R. L.; Wang, K. Chinese calligraphy inspired design of humidity/light dual responsive magic paper. *Adv. Mater. Technol.* **2021**, *6* (8), No. 2100044.

(10) Yao, S. S.; Yang, J.; Poblete, F. R.; Hu, X. G.; Zhu, Y. Multifunctional electronic textiles using silver nanowire composites. *ACS Appl. Mater. Interfaces* **2019**, *11* (34), 31028−31037.

(11) Zhang, Y.; Pan, C.; Liu, P.; Peng, L.; Liu, Z.; Li, Y.; Wang, Q.; Wu, T.; Li, Z.; Majidi, C.; et al. Coaxially printed magnetic mechanical electrical hybrid structures with actuation and sensing functionalities. *Nat. Commun.* **2023**, *14* (1), 4428.

(12) Dai, C. F.; Khoruzhenko, O.; Zhang, C. Q.; Zhu, Q. L.; Jiao, D. J.; Du, M.; Breu, J.; Zhao, P.; Zheng, Q.; Wu, Z. L. Magneto-orientation of magnetic double stacks for patterned anisotropic hydrogels with multiple responses and modulable motions. *Angew. Chem., Int. Ed.* **2022**, *61* (35), No. e202207272.

(13) Kim, Y.; Zhao, X. H. Magnetic soft materials and robots. *Chem. Rev.* **2022**, *122* (5), 5317−5364.

(14) Wang, T. L.; Ugurlu, H.; Yan, Y. B.; Li, M. T.; Li, M.; Wild, A. M.; Yildiz, E.; Schneider, M.; Sheehan, D.; Hu, W. Q.; et al. Adaptive wireless millirobotic locomotion into distal vasculature. *Nat. Commun.* **2022**, *13* (1), 4465.

(15) He, Z. W.; Satarkar, N.; Xie, T.; Cheng, Y. T.; Hilt, J. Z. Remote controlled multishape polymer nanocomposites with selective radiofrequency actuations. *Adv. Mater.* **2011**, *23* (28), No. 1100646.

(16) Sanchez, C. P.; Jerome, C. J.; Noels, L.; Vanderbemden, P. Review of Thermoresponsive Electroactive and magnetoactive shape memory polymer nanocomposites. *ACS Omega.* **2022**, *7*, 40701−40723.

(17) Ze, Q. J.; Kuang, X.; Wu, S.; Wong, J.; Montgomery, S. M.; Zhang, R. D.; Kovitz, J. M.; Yang, F. Y.; Qi, H. J.; Zhao, R. K. Magnetic shape memory polymers with integrated multifunctional shape manipulation. *Adv. Mater.* **2020**, *32* (4), No. 1906657.

(18) Behl, M.; Kratz, K.; Zotzmann, J.; Nochel, U.; Lendlein, A. Reversible bidirectional shape-memory polymers. *Adv. Mater.* **2013**, *25* (32), 4466−4469.

(19) Song, H. J.; Fang, Z. Z.; Jin, B. J.; Pan, P. J.; Zhao, Q.; Xie, T. Synergetic chemical and physical programming for reversible shape memory effect in a dynamic covalent network with two crystalline phases. *ACS Macro. Lett.* **2019**, *8* (6), 682−686.

(20) Zhang, H.; Yang, X.; Valenzuela, C.; Chen, Y. H.; Yang, Y. Z.; Ma, S. S.; Wang, L.; Feng, W. Wireless power transfer to electrothermal liquid crystal elastomer actuators. *ACS Appl. Mater. Interfaces* **2023**, *15* (22), 27195−27205.

(21) Oh, S.; Lee, S. W.; Byun, S. H.; Lee, S. M.; Kim, C. Y.; Yea, J.; Chung, S.; Li, S.; Jang, K. I.; Kang, J. H.; et al. 3D shape-morphing display enabled by electrothermally responsive, stiffness-tunable liquid metal platform with stretchable electroluminescent device. *Adv. Funct. Mater.* **2023**, *33* (24), No. 2214766.

(22) Liu, W. D.; Lei, Z. H.; Xing, W. K.; Xiong, J. C.; Zhang, Y. Y.; Tao, P.; Shang, W.; Fu, B. W.; Song, C. Y.; Deng, T. Enable multi-stimuli-responsive biomimetic actuation with asymmetric design of graphene-conjugated conductive polymer gradient film. *ACS Nano* **2023**, *17*, 16123−16134.

(23) Chen, J. C.; Cao, Y. T.; Pei, J. Y.; Zhao, H. Y. Multifunctional actuator based on graphene/PDMS composite materials with shape programmable configuration and high photothermal conversion capability. *ACS Appl. Mater. Interfaces* **2023**, *15* (26), 31917−31926.

(24) Huang, X. W.; Wei, J.; Wei, H.; Zhang, L. D. Magnetocaloric actuation of soft polymer robots. *J. Mater. Chem. C* **2021**, *9* (39), 13635−13639.

(25) Ma, Z. J.; Huang, Q. Y.; Xu, Q.; Zhuang, Q. N.; Zhao, X.; Yang, Y. H.; Qiu, H.; Yang, Z. L.; Wang, C.; Chai, Y.; et al. Permeable

superelastic liquid-metal fibre mat enables biocompatible and monolithic stretchable electronics. *Nat. Mater.* **2021**, *20* (6), 859−868.
(26) Bhuyan, P.; Wei, Y. W.; Sin, D.; Yu, J.; Nah, C.; Jeong, K. U.; Dickey, M. D.; Park, S. Soft and stretchable liquid metal composites with shape memory and healable conductivity. *ACS Appl. Mater. Interfaces* **2021**, *13* (24), 28916−28924.
(27) Zhu, L. F.; Chen, Y. Z.; Shang, W. H.; Handschuh-Wang, S.; Zhou, X. H.; Gan, T. S.; Wu, Q. X.; Liu, Y. Z.; Zhou, X. C. Anisotropic liquid metal-elastomer composites. *J. Mater. Chem. C* **2019**, *7* (33), 10166−10172.
(28) Fei, F.; Kotak, P.; He, L.; Li, X. F.; Vanderhoef, C.; Lamuta, C.; Song, X. Cephalopod-inspired stretchable self-morphing skin via embedded printing and twisted spiral artificial muscles. *Adv. Funct. Mater.* **2021**, *31* (46), No. 2105528.
(29) Wang, D. L.; Gao, C. Y.; Si, T. Y.; Li, Z. S.; Guo, B.; He, Q. Near-infrared light propelled motion of needlelike liquid metal nanoswimmers. *Colloids Surf., A* **2021**, *611*, No. 125865.
(30) Li, Q.; Liu, C.; Lin, Y.-H.; Liu, L.; Jiang, K.; Fan, S. Large-strain, multiform movements from designable electrothermal actuators based on large highly anisotropic carbon nanotube sheets. *ACS Nano* **2015**, *9* (1), 409−418.
(31) Chen, L.; Liu, C.; Liu, K.; Meng, C.; Hu, C.; Wang, J.; Fan, S. High-performance, low-voltage, and easy-operable bending actuator based on aligned carbon nanotube/polymer composites. *ACS Nano* **2011**, *5* (3), 1588−1593.
(32) Zhang, W.; Weng, M.; Zhou, P.; Chen, L.; Huang, Z.; Zhang, L.; Liu, C.; Fan, S. Transparency-switchable actuator based on aligned carbon nanotube and paraffin-polydimethylsiloxane composite. *Carbon* **2017**, *116*, 625−632.
(33) Chen, L. Z.; Weng, M. C.; Zhang, W.; Zhou, Z. W.; Zhou, Y.; Xia, D.; Li, J. X.; Huang, Z. G.; Liu, C. H.; Fan, S. S. Transparent actuators and robots based on single-layer superaligned carbon nanotube sheet and polymer composites. *Nanoscale* **2016**, *8* (12), 6877−6883.
(34) Cai, G.; Ciou, J.-H.; Liu, Y.; Jiang, Y.; Lee, P. S. Leaf-inspired multiresponsive MXene-based actuator for programmable smart devices. *Sci. Adv.* **2019**, *5* (7), No. eaaw7956.
(35) Ahn, J.; Jeong, Y.; Zhao, Z.-J.; Hwang, S.; Kim, K.; Ko, J.; Jeon, S.; Park, J.; Kang, H.; Jeong, J.-H.; et al. Heterogeneous conductance-based locally shape-morphable soft electrothermal actuator. *Adv. Mater. Technol.* **2020**, *5* (2), No. 1900997.
(36) Wu, G.; Wu, X.; Xu, Y.; Cheng, H.; Meng, J.; Yu, Q.; Shi, X.; Zhang, K.; Chen, W.; Chen, S. High-performance hierarchical black-phosphorous-based soft electrochemical actuators in bioinspired applications. *Adv. Mater.* **2019**, *31* (25), No. 1806492.
(37) Weng, M.; Duan, Y.; Zhou, P.; Huang, F.; Zhang, W.; Chen, L. Electric-fish-inspired actuator with integrated energy-storage function. *Nano Energy* **2020**, *68*, No. 104365.
(38) Tang, Z.-H.; Zhu, W.-B.; Mao, Y. Q.; Zhu, Z. C.; Li, Y. Q.; Huang, P.; Fu, S.-Y. Multiresponsive Ti3C2Tx MXene-based actuators enabled by dual-mechanism synergism for soft robotics. *ACS Appl. Mater. Interfaces* **2022**, *14* (18), 21474−21485.
(39) Zhang, X.; Tian, M.; Raza, T.; Zhao, H.; Wang, J.; Du, X.; Zhang, X.; Qu, L. Soft robotic reinforced by carbon fiber skeleton with large deformation and enhanced blocking forces. *Compos. B. Eng.* **2021**, *223*, No. 109099.
(40) Zhou, P.; Lin, J.; Zhang, W.; Luo, Z.; Chen, L. Pressure-perceptive actuators for tactile soft robots and visual logic devices. *Adv. Sci.* **2022**, *9* (5), No. 2104270.
(41) Zhang, Z. H.; Heron, J. T.; Pena-Francesch, A. Adaptive magnetoactive soft composites for modular and reconfigurable actuators. *Adv. Funct. Mater.* **2023**, *33*, No. 2215248.

https://doi.org/10.1021/acsnano.3c08888
ACS Nano 2023, 17, 24042−24054